IEEE Access
Multidisciplinary | Rapid Review | Open Access Journal

Received 20 February 2024, accepted 26 February 2024, date of publication 4 March 2024, date of current version 8 March 2024.

*Digital Object Identifier 10.1109/ACCESS.2024.3373044*

RESEARCH ARTICLE

# Upper-Limb Position-Robust Motion Recognition With Unsupervised Domain Adaptation

**SEJIN KIM AND WAN KYUN CHUNG, (Fellow, IEEE)**
Department of Mechanical Engineering, Pohang University of Science and Technology, Pohang-si 37673, South Korea

Corresponding author: Wan Kyun Chung (wkchung@postech.ac.kr)

This work was supported in part by the Industrial Strategic Technology Development Program (General purpose multi mode robot teaching device for difficult task where 0.1mm resolution of position and vel acc force teachings are essential) funded by the Ministry of Trade, Industry and Energy (MOTIE) of Korea under Grant 20009396; and in part by the Basic Science Research Program through the National Research Foundation of Korea (NRF) funded by the Ministry of Education under Grant 2020R1I1A2074953.

This work involved human subjects or animals in its research. Approval of all ethical and experimental procedures and protocols was granted by the Institutional Review Board of Pohang University of Science and Technology under Application No. PIRB-2023-E012.

**ABSTRACT** Upper-limb position is one of the most critical factors that degrade sEMG-based motion recognition accuracy. Therefore, we propose an upper-limb position-robust motion recognition with unsupervised domain adaptation. The proposed method finds the feature representation which reduces the difference between the distributions of labeled and unlabeled data acquired from the specific upper-limb position and other conditions respectively. It is shown that the proposed method has enhanced the classification accuracy by up to 13.50% compared to machine learning-based classifiers, convolutional neural network (CNN), and domain adversarial neural network (DANN). Especially, the lowest classification accuracy among every pair of training and test upper-limb positions has been improved by up to 19.96%. The effectiveness of the proposed method is also verified with the visualization of feature representation and comparison of a learning curve. To see the feasibility and performance in the real-world applications, we designed the virtual interface to control the ball in accordance with the real-time network estimation and conducted the following experiment: With the current ball position given, the subject has to reach the goal position as soon as possible while the error between desired and real trajectory is minimized at the same time. The proposed method has shown significantly higher reaching speed and tracking accuracy.

**INDEX TERMS** Deep learning, limb position effect, motion recognition, surface electromyogram (sEMG), unsupervised domain adaptation.

## I. INTRODUCTION

Surface electromyogram (sEMG) is a bioelectric signal which captures the motor unit action potential. Because sEMG is generated when muscles contract and is non-invasive, it is used to estimate the human intention in a variety of applications including virtual/augmented reality (VR/AR) [1], teleoperation [2], rehabilitation [3], and prosthesis control [4]. Especially, hand and wrist motion intentions are often considered because of their importance in daily living [5], [6], [7]. Pattern recognition is one of the most frequently used schemes to interpret the motion intention from sEMG and it was shown that several hand and wrist motions can be classified [8], [9], [10], [11], [12]. The primary assumption is that the sEMG patterns are stationary so that the patterns extracted from the training session will emerge in the later stages [13], [14], [15].

However, this assumption is not guaranteed when there exist the variations of the angles in arm joints. The length and shape of muscle are dependent on the joint angles and the corresponding shift between the muscle and electrode affects sEMG [16]. Furthermore, muscle activation

The associate editor coordinating the review of this manuscript and approving it for publication was Fahmi Khalifa.

© 2024 The Authors. This work is licensed under a Creative Commons Attribution-NonCommercial-NoDerivatives 4.0 License.
For more information, see https://creativecommons.org/licenses/by-nc-nd/4.0/

to produce the necessary force becomes different due to the force-length relationship of the muscle [17]. These joint angles are determined by the positioning of upper limb and consequently, changes in upper-limb position negatively affect pattern recognition.

To achieve upper-limb position-robust pattern recognition, labeled data are acquired from multiple upper-limb positions and an additional sensor is utilized. Fougner et al. [16] reported that if the labeled data are acquired from multiple upper-limb positions, classification accuracy is increased compared to the case with a single upper-limb position. Classification accuracy is even increased when the data from the accelerometer (ACC) attached to the forearm are included. Geng et al. [18] proposed the two-stage cascade classifier where ACC detects the upper-limb position and the corresponding sEMG classifier is applied to estimate the motion. The two-stage cascade classifier has shown higher mean classification accuracy compared to the classifier trained only with sEMG in five upper-limb positions. Williams et al. [19] proposed recurrent convolutional neural network for position-aware myoelectric prosthesis control. When labeled sEMG and ACC data from four upper-limb positions are used, classification accuracy was enhanced compared to the case where only labeled sEMG acquired from a single upper-limb position is used. However, the labeling process is time-consuming [20], [21], [22]. Furthermore, the attachment of an additional sensor might cause inconvenience and lower the usability.

To alleviate the burden of labeled data acquisition and using additional sensors, motion recognition with only sEMG from a single upper-limb position is considered. Khushaba et al. [23] proposed time-dependent spectral sEMG features which are designed to be invariant to translation, scaling, and amplification. Betthauser et al. [24] exploited an extreme learning machine with adaptive sparse representation classification (EASRC) which provides additional tolerance on interspersed data near classification boundaries and outliers from unexpected effect. However, these researches did not consider the distribution of data acquired from different upper-limb positions or propose the sEMG variation model with respect to upper-limb position. Therefore, it is hard to provide the generalized solution for upper-limb position-robust motion recognition.

Therefore, we propose a motion recognition with unsupervised domain adaptation. Given the labeled data from specific upper-limb position and unlabeled data from other positions, it aims to find the feature representation which aligns these two data distribution [25]. This allows to take into account the data distribution from various upper-limb positions and it is a differentiated advantage compared to the previous approaches which try to find the robust sEMG features or classifier only with the data from a single upper-limb position [23], [24]. Furthermore, unlabeled data do not need the labeling process so that the data acquisition becomes timely efficient. In this point of view, it can alleviate the burden of labeled data acquisition which is required in other previous works [16], [18], [19]. To the best of our knowledge, this is the first approach to apply the unsupervised domain adaptation for upper-limb position-robust motion recognition. The contributions of this study are as follows:

- We have shown the superiority of proposed method in classification accuracy over conventional machine learning-based classifiers, EASRC (adopted in [24]), convolutional neural network (CNN), and domain adversarial neural network (DANN) [26].
- We verified that the proposed method can align the distribution of labeled and unlabeled data. In addition, the effectiveness of the proposed method is clarified by comparing the learning curve to CNN and DANN.
- We analyzed the classification accuracy of the proposed method with respect to the amount of unlabeled data which is the important factor to determine the performance of unsupervised domain adaptation.
- To see the feasibility and performance in the real-world applications, we designed and conducted the real-time experiment where the subject moves the ball in the computer program according to the network inference and reach the goal as soon as possible. The performance of real-time experiment is quantified in terms of reaching speed and tracking accuracy.
- We analyzed the classification and tracking accuracy in each motion from the anatomical viewpoint and corresponding muscle activation.

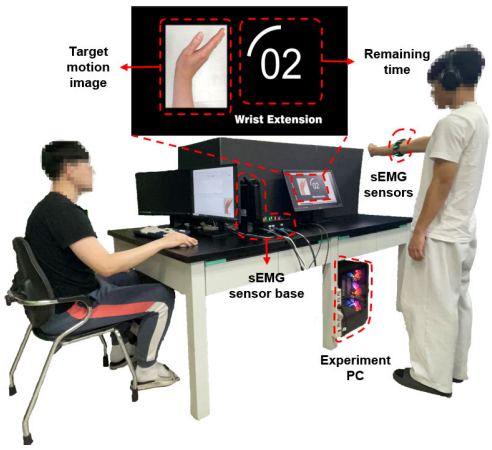


**FIGURE 1.** Experimental setup. By leveraging the customized program, experimenter controls the recording session and saves the acquired data whenever each session ends. In front of the subject, the monitor provides the visual cue comprised of target motion images and the remaining time.

This paper is organized as follows. Section II explains data acquisition, protocol, feature extraction, network structure, learning procedure, and detail information on implementation and performance comparison. Section III presents experimental results on classification accuracy and performance indices from real-time experiment. Section IV provides a discussion on experimental results with future works and Section V concludes this paper.

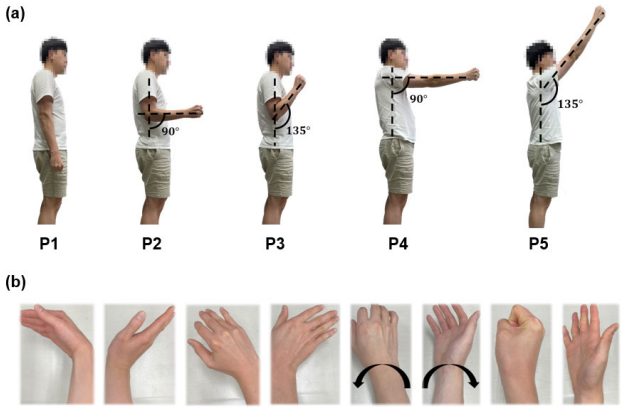


**FIGURE 2.** (a) Upper-limb positions to be considered. (b) Target motions to be classified. (From left to right) Wrist Flexion (WF), Wrist Extension (WE), Radial Deviation (RD), Ulnar Deviation (UD), Wrist Pronation (WP), Wrist Supination (WS), Hand Close (HC), and Hand Open (HO).

## II. METHODS

In the following sections, we will shorten unsupervised domain adaptation to domain adaptation. In addition, the set where labeled data are sampled is denoted as source domain, and that with the unlabeled data is named target domain [27]. Sec. II-A and Sec. II-B present the experiment setup and design. Sec. II-C to Sec. II-F explain the detail information on the proposed algorithm and its implementation. Sec. II-G introduces how the performance is quantified and compared.

### A. DATA ACQUISITION

After disinfecting the skin with alcohol swabs, the first sEMG sensor (Trigno wireless sEMG system, Delsys, USA) was attached to the muscle belly of the extensor carpi radialis while the other six sensors were equidistantly attached around the circumference of the forearm in a counterclockwise direction. As shown in Fig. 1, subjects stood and wore noise-canceling headphones to eliminate the effect of external sound. In addition, subject side was separated from the experimenter side so that the subjects can focus on the visual cues from the monitor in front of them.

Shoulder consists of three degrees of freedom (DoFs): flexion/extension, abduction/adduction, and internal/external rotation. In this study, we focused on shoulder flexion and extension because they are prevalent in the activities of daily living (ADL) [28] and determine the maximal shoulder rotation angle [29]. As elbow consists of one DoF with flexion and extension, sEMG was acquired in the following five upper-limb positions (Refer to Fig. 2. (a)) as follows:

P1) Straight arm hanging by the side.
P2) Straight upper arm and forearm forming an elbow angle of 90° with respect to the trunk.
P3) Straight upper arm and forearm forming an elbow angle of 135° with respect to the trunk.
P4) Straight arm forming an shoulder angle of 90° with respect to the trunk.
P5) Straight arm forming an shoulder angle of 135° with respect to the trunk.

Total eight hand and wrist motions in Fig. 2. (b) are considered. For wrist motions, wrist flexion (WF), wrist extension (WE), radial deviation (RD), ulnar deviation (UD), wrist pronation (WP), and wrist supination (WS) are included because they are required to modulate the hand orientation [30]. Additionally, we selected the hand close (HC) and hand open (HO) as these are frequently used to grasp and release the objects respectively [31]. The energy of sEMG is mainly focused below 500 Hz [32]. Therefore, to meet the Nyquist-Shannon sampling theorem, sEMG was acquired at a sampling frequency of 1 kHz. To alleviate the effects of signal distortion and artifacts, band-pass filter from 20 to 450 Hz [33] and notch filter on 60 Hz were applied.

### B. PROTOCOL

To compare the classification accuracy with other methods and analyze the effectiveness of domain adaptation with various conditions, offline experiment was held. Also, not only to verify the performance in a real-world application where the users dynamically take various actions according to visual feedback but also to show the feasibility of online neural network inference, a real-time experiment was conducted. Eleven subjects (all healthy and intact males, $23.6 \pm 1.3$ years old, $174.0 \pm 4.0$ cm, $68.7 \pm 10.1$ kg) and ten subjects (all healthy and intact males, $24.9 \pm 2.6$ years old, $173.8 \pm 5.7$ cm, $67.5 \pm 9.2$ kg) participated in the offline and real-time experiment respectively. The following protocols were explained to the subjects in advance and they provided their informed consent to participate. Whenever the subject reports muscle fatigue, the experiment was resumed after a sufficient break. The whole experiment is approved by the Institutional Review Board of Pohang University of Science and Technology (PIRB-2023-E012).

#### 1) OFFLINE EXPERIMENT

For every upper-limb position, the subjects maintained each motion for 5 seconds in the following order: WF, WE, RD, UD, WP, WS, HC, and HO. Before the subsequent contraction, 3 seconds were given for muscle relaxation. This was repeated for five times and between each repetition, the subject took a rest for 10 seconds. To minimize the muscle fatigue, the subjects were instructed to conduct the motion with moderate force. Contraction and relaxation timing were guided by visual cues from the monitor.

#### 2) REAL-TIME EXPERIMENT

The real-time experiment consists of three steps: 1) data acquisition, 2) network training, and 3) ball control session. Data acquisition was conducted in the same way as explained in Sec. II-B1, except that every motions were repeated four times for each upper-limb position. After the post-processing on acquired data, network training was held and the trained networks were utilized in ball control session. The goal of

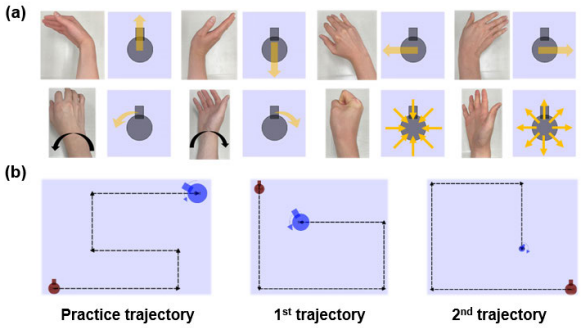


**FIGURE 3.** (a) Motions to be classified and corresponding ball movement. (b) Target trajectories in the ball control session.

ball control session is to reach the goal position by moving the ball according to the network inference. Before the experiment, subjects took a practice session to familiarize themselves with the control interface. Movement direction of the ball emulates that of hand and wrist so that subjects can be easily accustomed to the control interface (Refer to Fig. 3. (a)). Indeed, all subjects became familiar to the control interface within two trials of the practice session. After the practice session, each subject conducted the experiment in two trajectories for five upper-limb positions. As shown in Fig. 3. (b), each trajectory includes translation in all directions, while counterclockwise rotation and expansion are required in the first trajectory and clockwise rotation and shrinkage are to be held in the second trajectory. Each trial has a time limit of 75 seconds and the subjects can check the remaining time from right-upper corner of the window. If the time is over, then the program automatically stops. Between each trial, 30 seconds are given for muscle relaxation.

### C. FEATURE EXTRACTION

sEMG is a summation of stochastic motor unit action potentials [34] and various kinds of noises from environmental factors. Therefore, a sliding window is widely applied in various studies to extract useful features from multiple sEMG samples [35], [36], [37]. In this study, the length of a sliding window was set to 150 ms which corresponds to half of the maximal value for acceptable delay in system performance [38]. From the sliding window, we take advantage of following four time-domain features (TDF): mean absolute value (MAV), waveform length (WL), slope sign change (SSC), and zero crossing (ZC). While SSC and ZC include the frequency information, MAV and WL contain the energy and complexity information of sEMG respectively [39]. These features are distinctive [32] and requires simple calculation [40]. Especially, the simplicity of calculation is essential for the real-time implementation being within the scope of this study. The definition of each time domain feature is as follows:

- Mean absolute value (MAV) at time $t$ is given as follows:

$$MAV_i(t) = \frac{1}{N_w} \sum_{j=t-N_w+1}^{t} |x_i(j)| \tag{1}$$

where $i$ is the sEMG sensor index and $N_w$ is the size of a sliding window.

- Waveform length (WL) quantifies the waveform complexity of the sEMG segment in a sliding window. WL at time $t$ is given as follows:

$$WL_i(t) = \sum_{j=t-N_w+2}^{t} |x_i(j) - x_i(j-1)| \tag{2}$$

- Slope sign change (SSC) provides a kind of frequency measure. It is calculated as follows:

$$SSC_i(t) = \sum_{j=t-N_w+2}^{t-1} g_{ij} \tag{3}$$

where the function $g_{ij}$ is given as follows:

$$g_{ij} = \begin{cases} 1, & \text{if } \Delta x_i(j) \cdot \Delta x_i(j+1) < 0 \\ 0, & \text{otherwise} \end{cases} \tag{4}$$

- Zero crossing (ZC) provides another kind of frequency measure. It is calculated as follows:

$$ZC_i(t) = \sum_{j=t-N_w+2}^{t} h_{ij} \tag{5}$$

where the function $h_{ij}$ is given as follows:

$$h_{ij} = \begin{cases} 1, & \text{if } x_i(j) \cdot x_i(j-1) < 0 \\ 0, & \text{otherwise} \end{cases} \tag{6}$$

Englehart and Hudgins [41] argue that for SSC and ZC, $g_{ij}$ and $h_{ij}$ should include the threshold $\varepsilon$ to reduce the noise effect. However, Waris et al. [42] found that setting $\varepsilon$ to 0 provides a good trade-off between system performance and generalization. Therefore, $\varepsilon$ was not considered in this study. To alleviate the scale effect, each feature was normalized in the following way: MAV and WL were divided by the maximal value calculated from the acquired data while SSC and ZC were divided by the sliding window size. Since these four features are computed for each of the seven sEMG channels, the shape of the network input is (4, 7, 1).

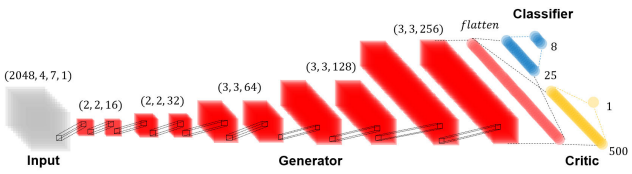


**FIGURE 4.** Overall network structure. Classifier and critic are connected to the flattened output of generator in parallel. Note that the numbers above the input and convolution layers denote the size of input and kernel. For the fully connected layers (FCLs), they denote the number of nodes.

### D. NETWORK STRUCTURE

The proposed method adopted Wasserstein-distance-guided representation learning (WDGRL) which is robust to gradient vanishing [43] and the network structure was modified to be optimal for our application. The network consists of 1) generator $f_g(\cdot)$, 2) classifier $f_c(\cdot)$, and 3) critic $f_{cr}(\cdot)$.

The goal of generator is to find the domain-independent representation from the input. It is comprised of ten convolution blocks where a 2D convolution layer with the stride of 1, batch normalization (BatchNorm), and rectified linear unit (ReLU) activation layer are connected in series. Here, max pooling is not adopted since the width of input is an odd number of 7. As shown in Fig. 4, first to fourth block use a (2, 2) size filter whereas the others use a (3, 3) size filter. This allows the network to focus on the relationship between adjacent elements in the earlier stage, and then explore global and representative characteristics of corresponding output. Inspired by the structure of VGG-16 [44], the number of convolution filters is doubled for every two blocks. Output of generator is flattened and becomes the input to the classifier.

Classifier consists of two fully connected layers (FCLs) with 25 and 8 (the number of motions to be classified) neurons. BatchNorm and ReLU follow each FCL and softmax activation is applied at the last layer to convert the output into probability.

Critic works as the estimator of Wasserstein distance between the probability distribution of source domain $\mathbb{P}_s$ and target domain $\mathbb{P}_t$ which is defined as follows [45]:

$$W(\mathbb{P}_s, \mathbb{P}_t) = \inf_{\gamma \in \Pi(\mathbb{P}_s, \mathbb{P}_t)} \mathbb{E}_{(x_s, x_t) \backsim \gamma} \left[ \| x_s - x_t \| \right] \tag{7}$$

Like the classifier, critic takes the flattened output of the generator as an input. It comprises two FCLs with 500 neurons and a single neuron, while the rest of the configuration is the same as that of the classifier. The number of nodes of the first FCL is set to be much larger than that of the classifier, allowing the network to be 1-Lipschitz among various alternatives.

### E. LEARNING PROCEDURE

It is intractable to calculate the infimum in (7) [45]. Therefore, from Kantorovich-Rubenstein duality, Wasserstein distance is alternatively calculated with a following equation [46]:

$$W(\mathbb{P}_s, \mathbb{P}_t) = \sup_{\|f_{cr}\|_L \leq 1} \mathbb{E}_{x \backsim \mathbb{P}_s}[f_{cr}\left(f_g\left(x\right)\right)] - \mathbb{E}_{x \backsim \mathbb{P}_t}[f_{cr}\left(f_g\left(x\right)\right)] \tag{8}$$

To restrict the critic to be 1-Lipschitz, gradient penalty term is added to the original cost function as follows [47]:

$$\begin{aligned} L_{cr} = {} & \mathbb{E}_{x \backsim \mathbb{P}_t}[f_{cr}(f_g\left(x\right))] - \mathbb{E}_{x \backsim \mathbb{P}_s}[f_{cr}\left(f_g\left(x\right)\right)] \\ & + \mathbb{E}_{\hat{x} \backsim \mathbb{P}_{\hat{x}}}[\left(\|\nabla_{\hat{x}} f_{cr}\left(f_g\left(\hat{x}\right)\right)\| - 1\right)^2] \end{aligned} \tag{9}$$

where $\hat{x} = \beta x_s + (1 - \beta) x_t$ is an interpolation between source and target domain data with $0 < \beta < 1$ and $\lambda$ is a Lagrangian multiplier. To enforce the unit gradient norm on critic, this is repeated for five times with random $\beta$ in each case. Next, generator and classifier are updated by categorical cross-entropy loss from the one-hot encoded label. This step is the same as conventional CNN learning. Lastly, generator is updated to minimize the estimated Wasserstein distance from critic with a following loss function:

$$L_g = \mathbb{E}_{x \backsim \mathbb{P}_s}[f_{cr}(f_g\left(x\right))] - \mathbb{E}_{x \backsim \mathbb{P}_t}[f_{cr}\left(f_g\left(x\right)\right)] \tag{10}$$

The overall procedure is illustrated in Fig. 5.

### F. IMPLEMENTATION

#### 1) OFFLINE EXPERIMENT

Conventional machine learning-based classifiers and EASRC were implemented with MATLAB R2020b and the computer equipped with Intel(R) Core(TM) i7-10700K CPU and 48GB of RAM was utilized. For EASRC, we used the difference tolerance of the two largest entries $\alpha$ of 0.1, regularization parameter $\lambda$ of 0.0005, and the number of hidden nodes $L$ of 1000 respectively [48].

CNN, DANN, and the proposed method were implemented with Tensorflow and Keras API while the training was conducted on a computer equipped with 2 $\times$ NVIDIA GeForce RTX 3090 GPU and 128GB of RAM. CNN structure was set to the concatenation of generator and classifier of the proposed method. The generator of DANN had the same structure with the proposed method while the classifier and discriminator were comprised of 3 FCLs with the size of (250, 50, 8) and (500, 100, 2) respectively. This was because this structure had shown the highest classification accuracy among various candidates. Every network was trained for 350 epochs with ADAM optimizer, batch size of 2048, and learning rate of 0.00001. For the loss function, categorical accuracy was used in classifier (for every network) and discriminator (only in DANN) while $L_{cr}$ in (9) was used in critic (only in the proposed method).

#### 2) REAL-TIME EXPERIMENT

Data acquisition and ball control session were held on the computer equipped with Intel(R) Core(TM) i5-12600K CPU, 16GB of RAM, and NVIDIA GeForce GTX 1080 Ti GPU while network training was conducted on the same equipment as the offline experiment. The structure and training configuration of each network were the same as described in II-F1, except that the epoch and learning rate were set to 100 and 0.00003 respectively. This is to reduce the time difference between data acquisition and ball control session so that the subjects maintain same physiological state. For the ball control session, the program including data processing and neural network inference was implemented with the framework illustrated in Fig. 6. First, to guarantee that data processing which involves data acquisition and feature extraction is held within 1 millisecond (ms), Beckhoff TwinCAT was utilized as a real-time operating system (RTOS). Second, for high-speed neural network inference,

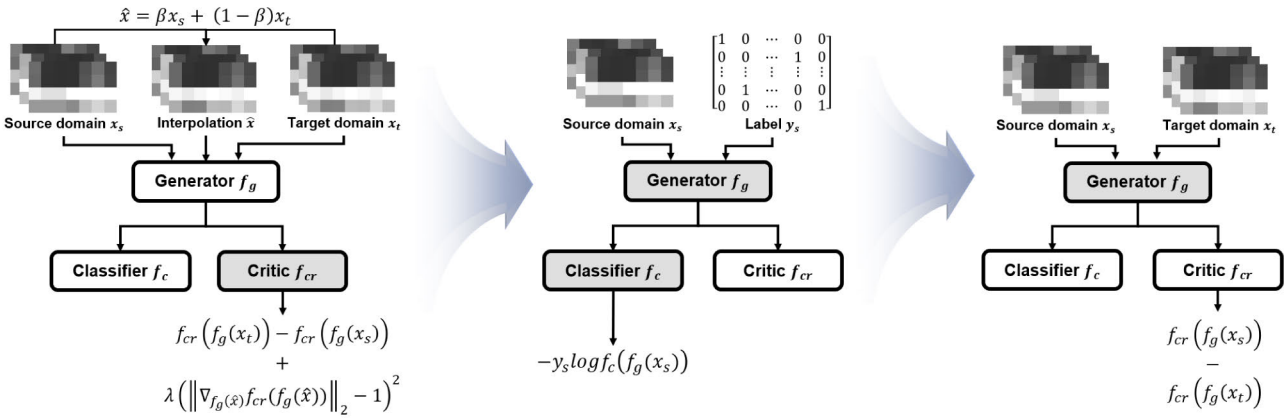


**FIGURE 5.** Schematic illustration of the learning procedure. (First step) Critic is updated to estimate the Wasserstein distance. (Second step) Generator and classifier are updated to minimize the categorical cross-entropy loss. This step aims to maximize the classification accuracy of labeled data used for training. (Third step) Generator is updated to minimize the Wasserstein distance estimated from the critic. These three steps are all held within an iteration. In each step, the components to be updated are shaded in gray and the loss function to be calculated is presented.

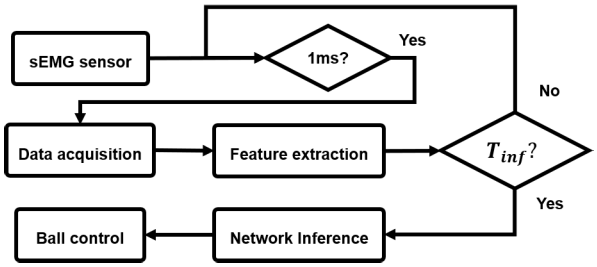


**FIGURE 6.** Framework for ball control session.

NVIDIA TensorRT SDK was applied. Inference was held every $T_{inf}$ which was set to 15 ms in this study, and that result was used to move the ball accordingly. Data processing and network inference were implemented as asynchronous threads so that they run in parallel and do not interfere with each operation.

### G. PERFORMANCE COMPARISON

#### 1) OFFLINE EXPERIMENT

The performance is quantified by classification accuracy and that of the proposed method is compared to 1) conventional machine learning-based classifiers, 2) EASRC, 3) CNN, and 4) DANN. Conventional machine learning-based classifiers include linear discriminant analysis (LDA) [49], [50], [51], k-nearest neighbors (k-NN) [52], [53], and support vector machine (SVM) [54], [55], [56] which are widely applied in the sEMG-based intention recognition. EASRC [24] is compared because it is adopted in the related works and CNN [57], [58], [59] works as a baseline of the proposed method because it is trained without the unlabeled data. Lastly, from DANN [60], [61], the effectiveness of using Wasserstein distance in domain adaptation can be evaluated because it utilizes the discriminator to figure out whether the data come from source or target domain instead of critic. For intra-position cases, 5-fold cross validation is applied because each contraction is repeated for five times. The total data except one specific trial are used for training while the remainder is kept for validation. This is held for every repetition and the mean classification accuracy is adopted. For inter-position cases, whole labeled data from the source domain are used for training while unlabeled data from the target domain are additionally employed for DANN and the proposed method.

#### 2) REAL-TIME EXPERIMENT

Three kinds of neural networks are compared: CNN, DANN, and the proposed network. There are two reasons why these networks are selected. First, the effect of domain adaptation can be seen by comparing CNN which does not require target domain data while other networks do. Second, the effect of using Wasserstein distance can be seen from the comparison to DANN. DANN and the proposed network was trained by using the labeled data from P1 and the unlabeled data from other upper-limb positions whereas only the labeled data from P1 are necessary for CNN. This is because P1 is the least affected by the gravitational effect.

To quantify the performance of a ball control session, two metrics are calculated: One is throughput (TP) and the other is path efficiency (PE). First, TP quantifies the speed of reaching the goal position and is defined as follows [62]:

$$TP = \frac{ID}{MT} = \frac{log_2\left(\sum_{m\in\{X,Y,Rotation,Scale\}} \frac{L_m}{W_m} + 1\right)}{MT} \quad (11)$$

where $ID$ is the index of difficulty, $MT$ is the movement time, $L_m$ and $W_m$ are the length and tolerance of the $m$th direction respectively. On the other hand, PE quantifies how well the desired trajectory is followed to reach the goal position and is defined as follows [63]:

$$PE = \frac{1}{\sum_{m\in\{X,Y,Rotation,Scale\}} \left|\frac{L_{real_m}}{L_{des_m}} - 1\right|} \quad (12)$$

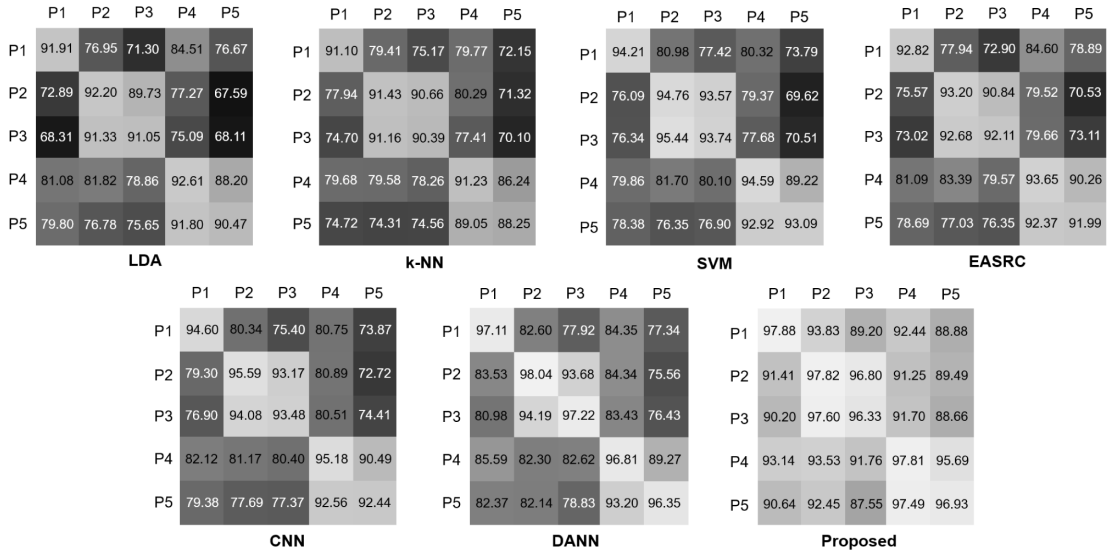


**FIGURE 7.** Classification accuracy (in %) from every pair of training and test upper-limb positions averaged across all subjects and motions. Each row and column represents training and test upper-limb position respectively. Lighter color indicates higher accuracy. For visual explicitness, accuracy under 80% is represented with white letters while others are represented with black.

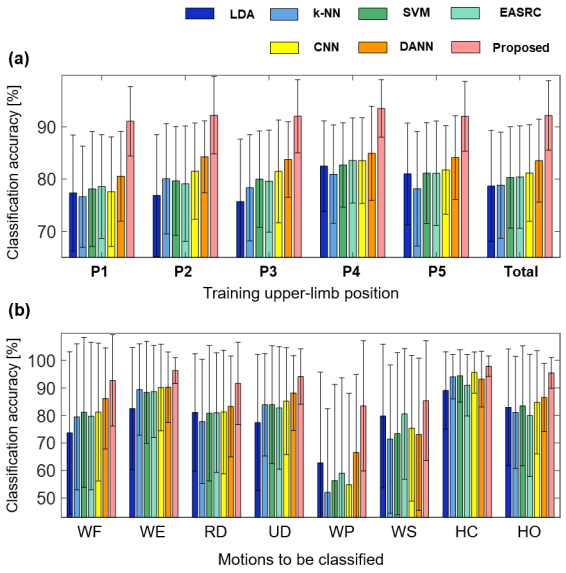


**FIGURE 8.** (a) Target domain classification accuracy with respect to upper-limb position averaged across all subjects and motions. (b) Target domain classification accuracy with respect to motion averaged across all subjects and upper-limb positions.

where $L_{real_m}$ and $L_{des_m}$ are the length in the $m$th direction of the desired and real trajectory respectively. To make the value larger when the real trajectory is closer to the desired trajectory, the reciprocal is taken instead of the original definition. In order to check how well the intention is captured for each DoF in ball control session, we also define the path efficiency of each direction $m \in \{X, Y, Rotation, Scale\}$ as follows:

$$PE_m = \frac{1}{|\frac{L_{real_m}}{L_{des_m}} - 1|} \tag{13}$$

## III. EXPERIMENTAL RESULTS

### A. OFFLINE EXPERIMENT

#### 1) CLASSIFICATION ACCURACY

The performance of the proposed method is validated on every pair of upper-limb positions as presented in Fig. 7. The lowest mean classification accuracy of the proposed method is 87.55% (when it is trained in P5 and tested in P3), which is 19.96%, 17.44%, 17.93%, 17.01%, 14.83%, and 11.99% higher than those of LDA, k-NN, SVM, EASRC, CNN, and DANN respectively. It is notable that regardless of the classifier, the classification accuracy is relatively higher when the same joint movement is involved in the training and test data. For example, the classifier trained with P2 shows relatively high classification accuracy on P3 and vice versa. From these results, it can argued that the upper-limb joint configuration determines the variations on sEMG.

In addition, the proposed method achieves the highest mean classification accuracy in every training upper-limb position as shown in Fig. 8. (a). There is a significant enhancement on the total classification accuracy ($p < 0.001$) with an amount of 13.50%, 13.36%, 11.86%, 11.78%, 11.01%, and 8.65% compared to LDA, k-NN, SVM, EASRC, CNN, and DANN respectively. In addition, the proposed method has shown the highest mean classification accuracy for every class as presented in Fig. 8. (b). Especially, among eight classes, it shows the largest enhancement in WP and WS with an amount of 16.87% and 12.22% compared to DANN.

#### 2) FEATURE REPRESENTATION

Feature representations from CNN, DANN, and the proposed method are visualized using t-SNE and the results are shown in Fig. 9. In the case of CNN, the distributions from the source and target domain are not aligned and especially, data

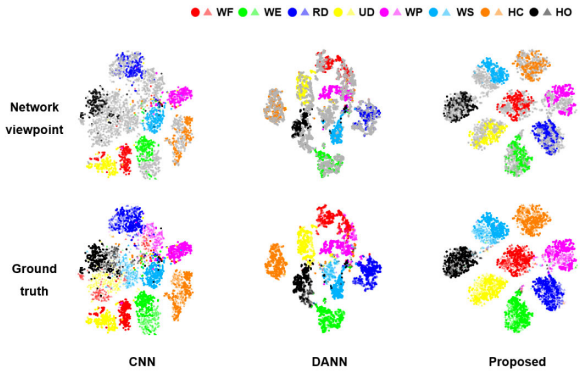


**FIGURE 9.** Visualization of features extracted from the generator of each network. (Top row) As the network does not know the label, all target domain data are grayed out. (Bottom row) Features from source and target domain are represented as circles with thicker color and triangles with lighter color respectively.

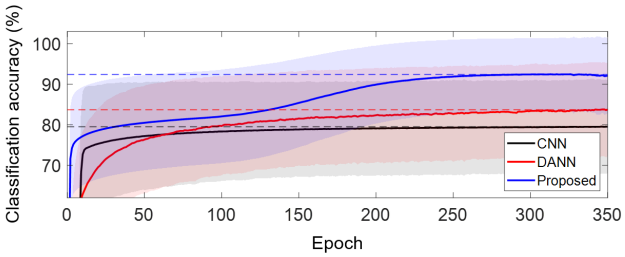


**FIGURE 10.** Learning curves of CNN, DANN, and the proposed method averaged across all subjects and motions in target domain. Shaded area and dashed line represent standard deviation and the converging classification accuracy respectively.

distributions of WF, UD, WP, and WS differ the most. This is because the target domain data were not considered in the learning process. On the other hand, with DANN, most of the distributions from WF and UD are aligned and the effect of domain adaptation is clearly shown in this comparison. However, some of the target domain data, such as WP and WS, are not aligned yet.

In the case of the proposed method, two distributions are aligned in every region so that the classifier which is optimized for the source domain can be also utilized in the target domain. This result shows that the proposed method is the most effective way to learn how to extract domain-invariant features.

#### 3) LEARNING CURVE

Fig. 10 shows the learning curve of CNN, DANN, and the proposed method averaged across every subject and upper-limb position with respect to target domain data. Because CNN does not consider the target domain data, it achieves the final classification accuracy of 79.48% which is the lowest among three networks. DANN achieves the final classification accuracy of 83.76% which is 4.28% higher than CNN. Interestingly, classification accuracy of DANN is lower than that of CNN before 70 iterations. Therefore,

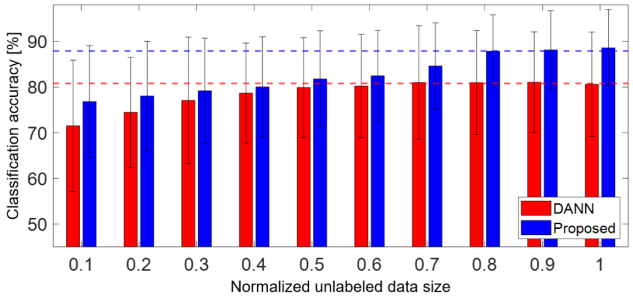


**FIGURE 11.** Target domain classification accuracy with respect to the normalized unlabeled data size. The convergence value of the target domain classification accuracy is represented with a dashed line.

we speculate that domain-invariant and class-distinguishable feature extraction in DANN are adversarial to each other in the earlier stage.

On the other hand, the proposed method has shown more complicated aspect and it is divided into three phases: 1) exploration, 2) adaptation, and 3) convergence. In the exploration phase, target domain classification accuracy is maintained or slightly increasing, meaning that the network tries to explore various conditions to find the optimal parameters. In the adaptation phase, target domain classification accuracy is increasing so that network begins to converge to the optimal parameters which has been explored in the previous phase. It is notable that the classification accuracy accuracy is enhanced with an amount of 10.40% in this phase. Finally, in the convergence phase, it reaches the plateau and achieves the final classification accuracy of 92.43% which is higher than CNN and DANN with an amount of 12.95% and 8.67% respectively.

#### 4) THE EFFECT OF TARGET DOMAIN DATA SIZE

Fig. 11 shows the target domain classification accuracy with respect to the size of unlabeled target domain data, which is normalized to the total length of 189,840. The normalized data size ranges from 0.1 to 1 and is incremented by 0.1. In the case of DANN, it reaches a plateau at the normalized data size of 0.7 and converges to 80.76%. On the other hand, the proposed method reaches a plateau at the normalized data size of 0.8 and converges to 87.86%. Therefore, the certain amount of target domain data, which ranges from about 132,900 to 151,900 data points, is necessary for the convergence given that the network structure to be utilized is comparable to that in this study. In addition, it is notable that regardless of the data size, the classification accuracy of the proposed method was higher than DANN. From this result, it can be inferred that the proposed method is more effective than DANN even when the sufficient data acquisition is not available.

### B. REAL-TIME EXPERIMENT

#### 1) ITERATION TIME

As shown in Fig. 12. (a), iteration time for data processing does not exceed the acceptable time of 1 ms with the

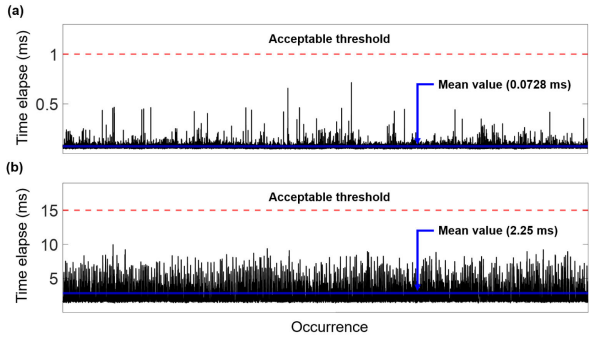


**FIGURE 12.** Iteration time for (a) data processing and (b) neural network inference.

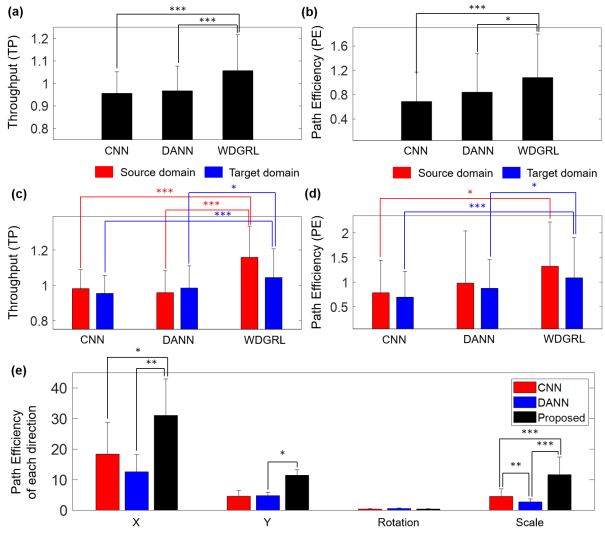


**FIGURE 13.** (a) Total throughput and (b) total path efficiency averaged across all subjects and upper-limb positions. (c) Throughput and (d) path efficiency from source and target domain averaged across all subjects. (e) Path efficiency of each direction (X, Y, Rotation, Scale). Note that $*$, $**$, and $***$ represent $p < 0.05$, $p < 0.01$, and $p < 0.001$ respectively.

average value of 0.0728 ms. This result shows that the system guarantees the sampling rate of 1 kHz and satisfies the Nyquist criterion to reconstruct the sEMG within the frequency range of 500 Hz. Furthermore, Fig. 12. (b) shows that the iteration time for neural network inference is less than 15 ms and no delay or runtime error does not occur during the ball control session. The mean iteration time for neural network inference is 2.25 ms which is much lower than the optimal controller delay threshold of 100 ms [64]. Based on this result, it can be argued that the proposed method can also be applied in real-time operation without delay-related performance degradation.

### 2) PERFORMANCE INDICES

Fig. 13. (a) shows the TP and PE of CNN, DANN, and the proposed method. First, proposed method has shown significantly higher TP than other networks. It means that the goal position was reached faster in a certain trajectory and the user controlled the interface with minimal effort. Also, in Fig. 13. (b), proposed method has shown significantly higher PE than other networks and it indicates that the intention was accurately recognized.

The aspects of each PI in source and target domain are also analyzed. In Fig. 13. (c), it can be shown that WDGRL has the highest TP regardless of the domain. It indicates that if robustness on the target domain is not secured, the performance in the source domain might also be low. Interestingly, there is no significant difference on TP between CNN and DANN. Based on the results of III-A2, we can speculate that if some distributions are not aligned from the domain adaptation, then performance enhancement cannot be guaranteed. In Fig. 13. (d), it is shown that the proposed method has the highest PE regardless of the domain. Although it has a $p$-value of 0.0628 against DANN for the source domain, the other cases show significant differences ($p < 0.05$). Furthermore, given that the PE of proposed method in the target domain is higher than that of the source domain from other networks, it can be argued that the performance in the source domain may also be lower if robustness on the target domain is not secured.

In case of the PE of each direction, the proposed method has outperformed CNN and DANN in every movement direction except rotation as shown in Fig. 13. (e). It is remarkable that the PE of rotation is much lower than those of X, Y, and scaling. The reason why this phenomenon happens is analyzed in Sec. IV.

### 3) TRAJECTORY COMPARISON

To support the PI results in Sec. III-B2, some examples of desired and real trajectory are also visualized in Fig. 14. Since the ball control interface has four degrees-of-freedoms (DoFs), the movement in X and Y direction is plotted in one graph while rotation and scaling are plotted in the other graph. The tolerance to determine whether the goal position was reached is also displayed in a dashed line. For the source domain, it is shown that the goal position is reached the fastest with the proposed method. For the target domain, the real trajectory from other networks deviates from the desired trajectory. On the other hand, with the proposed method, desired trajectory is followed more accurately and the ball arrives at the goal position within the time limit.

## IV. DISCUSSION

From Sec. III-A1, it is shown that the classification accuracy from WP and WS are the lowest among eight motions. In addition, as presented in Sec. III-B2, rotation has a significantly lower PE compared to translation in the X, Y direction or scaling. To understand why it is more difficult to recognize WP and WS than others, we need to consider the characteristics of the forearm muscles involved in these motions. For movements involved in translation and scaling, the agonist (e.g., flexor carpi radialis for wrist flexion) is not only a superficial muscle but also relatively large so that the signal amplitude becomes high. However, the situation

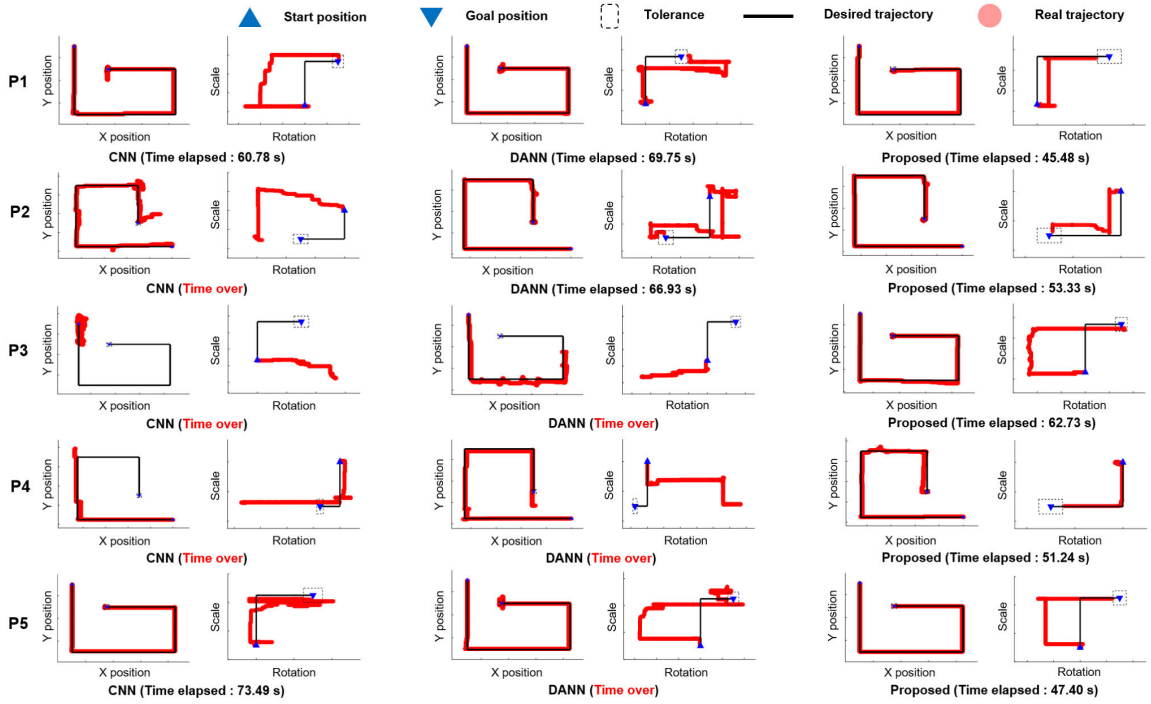


**FIGURE 14.** Desired and real trajectory in source (P1) and target domain (P2, P3, P4, P5). The symbols for start position, goal position, tolerance, desired trajectory, and real trajectory are given at the top. For each case, two figures are presented: Left figure shows the movement in X and Y direction while the movement in rotation and scaling is drawn in the right figure. The time elapsed for the ball to travel from the start position to the goal position is denoted under the graph.

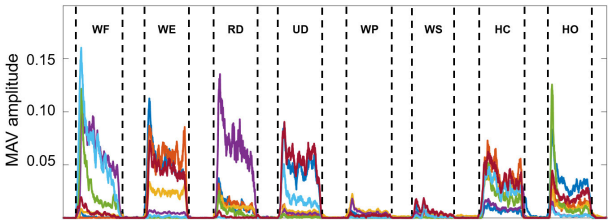


**FIGURE 15.** An example of sEMG mean absolute value (MAV).

becomes different when it comes to the WP or WS. WP has two agonists: One is a pronator quadratus and the other is a pronator teres. The pronator quadratus is a deep muscle which is difficult to obtain a strong signal. Even though the pronator teres is a superficial muscle, it is relatively smaller than adjacent muscles so that the signal is hard to be acquired. A supinator, which is involved in WS, is also a deep muscle so that it is difficult to get a strong signal. As shown in Fig. 15, MAV amplitudes from WP and WS are lower than others. Hence, contrary to other motions, the effects of upper-limb position change on sEMG become significant. In other words, it indicates that the classification margin between WP and WS is relatively small and the sEMG deviation from these effects becomes larger. As a result, classifiers are likely to confuse these two motions and this is supported by the fact that WS possesses the highest portion among the wrong estimation of WP, and vice versa.

This study will be further extended by the following considerations. First, we dealt with five static upper-limb positions from the flexion and extension of shoulder and elbow. However, other upper-limb positions with abduction, adduction, internal rotation, and external rotation of shoulder may also affect the sEMG patterns. Furthermore, the sEMG patterns are likely to be influenced by dynamic upper-limb movement and gravitational effect. In the future works, robustness on these conditions will be considered. Second, as well as HC and HO, various grasping motions will be considered. For example, lateral and tripod grip are necessary to grasp thin and small objects. As the grasping motions require the coordination of fingers, sEMG patterns from each finger movement should be distinguishable. However, fingers are controlled by the multi-tendoned muscles such as flexor digitorum superficialis [65] or extensor digitorum communis [66] so that the corresponding sEMG patterns are largely overlapped. Therefore, we will think over the usage of high-density electrode array to enhance the spatial resolution of sEMG. Lastly, the experiment was only held on healthy and intact subjects. Therefore, we will also verify the effectiveness of the proposed method for patients with muscle weakness or transradial amputees.

## V. CONCLUSION

This study proposes the sEMG-based motion recognition robust to upper-limb position change with unsupervised domain adaptation. The target domain classification accuracy

is significantly improved because the proposed method can align the source and target domain as shown from the visualization of feature representation. Also, the proposed method has shown significantly higher TP and PE than CNN and DANN ($p < 0.05$) in the real-time experiment. It means that the goal position is reached faster and more accurately on a given trajectory so that the user can control the interface with minimal effort. Especially, it is remarkable that TP and PE of the proposed method in the target domain are higher than those of other networks in the source domain. Therefore, we expect that this study may reduce the rejections in various applications due to frequent misclassifications from the upper-limb position change.

## REFERENCES

[1] A. Dwivedi, Y. Kwon, and M. Liarokapis, "EMG-based decoding of manipulation motions in virtual reality: Towards immersive interfaces," in *Proc. IEEE Int. Conf. Syst., Man, Cybern. (SMC)*, Toronto, ON, Canada, Oct. 2020, pp. 3296–3303.

[2] A. Dwivedi, G. Gorjup, Y. Kwon, and M. Liarokapis, "Combining electromyography and fiducial marker based tracking for intuitive telemanipulation with a robot arm hand system," in *Proc. 28th IEEE Int. Conf. Robot Human Interact. Commun. (RO-MAN)*, New Delhi, India, Oct. 2019, pp. 1–6.

[3] S. R. Chang, N. Hofland, Z. Chen, C. Tatsuoka, L. G. Richards, M. Bruestle, H. Kovelman, and J. Naft, "Myoelectric arm orthosis assists functional activities: A 3-month home use outcome report," *Arch. Rehabil. Res. Clin. Transl.*, vol. 5, no. 3, Sep. 2023, Art. no. 100279.

[4] K. Z. Zhuang, N. Sommer, V. Mendez, S. Aryan, E. Formento, E. D'Anna, F. Artoni, F. Petrini, G. Granata, G. Cannaviello, W. Raffoul, A. Billard, and S. Micera, "Shared human–robot proportional control of a dexterous myoelectric prosthesis," *Nature Mach. Intell.*, vol. 1, no. 9, pp. 400–411, Sep. 2019.

[5] E. Pezent, C. G. Rose, A. D. Deshpande, and M. K. O'Malley, "Design and characterization of the OpenWrist: A robotic wrist exoskeleton for coordinated hand-wrist rehabilitation," in *Proc. Int. Conf. Rehabil. Robot. (ICORR)*, London, U.K., Jul. 2017, pp. 720–725.

[6] Z. Guo, S. Zhou, K. Ji, Y. Zhuang, J. Song, C. Nam, X. Hu, and Y. Zheng, "Corticomuscular integrated representation of voluntary motor effort in robotic control for wrist-hand rehabilitation after stroke," *J. Neural Eng.*, vol. 19, no. 2, Mar. 2022, Art. no. 026004.

[7] M. Dragusanu, M. Z. Iqbal, T. L. Baldi, D. Prattichizzo, and M. Malvezzi, "Design, development, and control of a hand/wrist exoskeleton for rehabilitation and training," *IEEE Trans. Robot.*, vol. 38, no. 3, pp. 1472–1488, Jun. 2022.

[8] A. Soares, A. Andrade, E. Lamounier, and R. Carrijo, "The development of a virtual myoelectric prosthesis controlled by an EMG pattern recognition system based on neural networks," *J. Intell. Inf. Syst.*, vol. 21, no. 2, pp. 127–141, Sep. 2003.

[9] A. B. Ajiboye and R. F. Weir, "A heuristic fuzzy logic approach to EMG pattern recognition for multifunctional prosthesis control," *IEEE Trans. Neural Syst. Rehabil. Eng.*, vol. 13, no. 3, pp. 280–291, Sep. 2005.

[10] E. Scheme and K. Englehart, "Electromyogram pattern recognition for control of powered upper-limb prostheses: State of the art and challenges for clinical use," *J. Rehabil. Res. Develop.*, vol. 48, no. 6, pp. 643–660, 2011.

[11] X. Chen, D. Zhang, and X. Zhu, "Application of a self-enhancing classification method to electromyography pattern recognition for multifunctional prosthesis control," *J. Neuroeng. Rehabil.*, vol. 10, no. 1, pp. 1–13, May 2013.

[12] L. Resnik, H. Huang, A. Winslow, D. L. Crouch, F. Zhang, and N. Wolk, "Evaluation of EMG pattern recognition for upper limb prosthesis control: A case study in comparison with direct myoelectric control," *J. Neuroeng. Rehabil.*, vol. 15, no. 1, pp. 1–13, Mar. 2018.

[13] K. Xing, P. Yang, J. Huang, Y. Wang, and Q. Zhu, "A real-time EMG pattern recognition method for virtual myoelectric hand control," *Neurocomputing*, vol. 136, pp. 345–355, Jul. 2014.

[14] A. Phinyomark, F. Quaine, S. Charbonnier, C. Serviere, F. Tarpin-Bernard, and Y. Laurillau, "Feature extraction of the first difference of EMG time series for EMG pattern recognition," *Comput. Methods Programs Biomed.*, vol. 117, no. 2, pp. 247–256, Nov. 2014.

[15] J. He, D. Zhang, N. Jiang, X. Sheng, D. Farina, and X. Zhu, "User adaptation in long-term, open-loop myoelectric training: Implications for EMG pattern recognition in prosthesis control," *J. Neural Eng.*, vol. 12, no. 4, Jun. 2015, Art. no. 046005.

[16] A. Fougner, E. Scheme, A. D. C. Chan, K. Englehart, and Ø. Stavdahl, "Resolving the limb position effect in myoelectric pattern recognition," *IEEE Trans. Neural Syst. Rehabil. Eng.*, vol. 19, no. 6, pp. 644–651, Dec. 2011.

[17] G. A. Mohammed and M. Hou, "Optimization of active muscle force–length models using least squares curve fitting," *IEEE Trans. Biomed. Eng.*, vol. 63, no. 3, pp. 630–635, Mar. 2016.

[18] Y. Geng, P. Zhou, and G. Li, "Toward attenuating the impact of arm positions on electromyography pattern-recognition based motion classification in transradial amputees," *J. Neuroeng. Rehabil.*, vol. 9, no. 1, pp. 1–11, Oct. 2012.

[19] H. E. Williams, A. W. Shehata, M. R. Dawson, E. Scheme, J. S. Hebert, and P. M. Pilarski, "Recurrent convolutional neural networks as an approach to position-aware myoelectric prosthesis control," *IEEE Trans. Biomed. Eng.*, vol. 69, no. 7, pp. 2243–2255, Jul. 2022.

[20] H. Wang, P. Huang, T. Xu, G. Li, and Y. Hu, "Towards zero retraining for multiday motion recognition via a fully unsupervised adaptive approach and fabric myoelectric armband," *IEEE Trans. Neural Syst. Rehabil. Eng.*, vol. 30, pp. 217–225, 2022.

[21] N. Zheng, Y. Li, W. Zhang, and M. Du, "User-independent EMG gesture recognition method based on adaptive learning," *Frontiers Neurosci.*, vol. 16, pp. 1–13, Mar. 2022.

[22] R. Soroushmojdehi, S. Javadzadeh, A. Pedrocchi, and M. Gandolla, "Transfer learning in hand movement intention detection based on surface electromyography signals," *Frontiers Neurosci.*, vol. 16, pp. 1–18, Nov. 2022.

[23] R. N. Khushaba, M. Takruri, J. V. Miro, and S. Kodagoda, "Towards limb position invariant myoelectric pattern recognition using time-dependent spectral features," *Neural Netw.*, vol. 55, pp. 42–58, Jul. 2014.

[24] J. L. Betthauser, C. L. Hunt, L. E. Osborn, M. R. Masters, G. Lévay, R. R. Kaliki, and N. V. Thakor, "Limb position tolerant pattern recognition for myoelectric prosthesis control with adaptive sparse representations from extreme learning," *IEEE Trans. Biomed. Eng.*, vol. 65, no. 4, pp. 770–778, Apr. 2018.

[25] O. Sener, H. O. Song, A. Saxena, and S. Savarese, "Learning transferrable representations for unsupervised domain adaptation," in *Proc. Adv. Neural Inf. Process. Syst.*, vol. 29, Dec. 2016, pp. 1–9.

[26] Y. Ganin, E. Ustinova, H. Ajakan, P. Germain, G. Larochelle, F. Laviolette, M. Marchand, and V. Lempitsky, "Domain-adversarial training of neural networks," *J. Mach. Learn. Res.*, vol. 17, no. 1, pp. 2030–2096, Apr. 2016.

[27] S. Ben-David, J. Blitzer, K. Crammer, and F. Pereira, "Analysis of representations for domain adaptation," in *Proc. Adv. Neural Inf. Process. Syst.*, vol. 19, Vancouver, BC, Canada, Dec. 2006, pp. 1–8.

[28] A. M. Oosterwijk, M. K. Nieuwenhuis, C. P. van der Schans, and L. J. Mouton, "Shoulder and elbow range of motion for the performance of activities of daily living: A systematic review," *Physiotherapy Theory Pract.*, vol. 34, no. 7, pp. 505–528, Jan. 2018.

[29] D. J. Magermans, E. K. J. Chadwick, H. E. J. Veeger, and F. C. T. van der Helm, "Requirements for upper extremity motions during activities of daily living," *Clin. Biomech.*, vol. 20, no. 6, pp. 591–599, Jul. 2005.

[30] J. Fan, J. He, and S. I. H. Tillery, "Control of hand orientation and arm movement during reach and grasp," *Exp. Brain Res.*, vol. 171, no. 3, pp. 283–296, Nov. 2005.

[31] I. M. Bullock, J. Z. Zheng, S. De La Rosa, C. Guertler, and A. M. Dollar, "Grasp frequency and usage in daily household and machine shop tasks," *IEEE Trans. Haptics*, vol. 6, no. 3, pp. 296–308, Jul. 2013.

[32] A. Phinyomark, P. Phukpattaranont, and C. Limsakul, "Feature reduction and selection for EMG signal classification," *Expert Syst. Appl.*, vol. 39, no. 8, pp. 7420–7431, Jun. 2012.

[33] C. J. De Luca, L. D. Gilmore, M. Kuznetsov, and S. H. Roy, "Filtering the surface EMG signal: Movement artifact and baseline noise contamination," *J. Biomech.*, vol. 43, no. 8, pp. 1573–1579, May 2010.

[34] A. Merlo, D. Farina, and R. Merletti, "A fast and reliable technique for muscle activity detection from surface EMG signals," *IEEE Trans. Biomed. Eng.*, vol. 50, no. 3, pp. 316–323, Mar. 2003.

[35] J.-U. Chu, I. Moon, and M.-S. Mun, "A real-time EMG pattern recognition system based on linear-nonlinear feature projection for a multifunction myoelectric hand," *IEEE Trans. Biomed. Eng.*, vol. 53, no. 11, pp. 2232–2239, Nov. 2006.
[36] Q. Meng, J. Zhang, and X. Yang, "Virtual rehabilitation training system based on surface EMG feature extraction and analysis," *J. Med. Syst.*, vol. 43, no. 3, pp. 1–11, Jan. 2019.
[37] J. Liu, Y. Ren, D. Xu, S. H. Kang, and L.-Q. Zhang, "EMG-based real-time linear-nonlinear cascade regression decoding of shoulder, elbow, and wrist movements in able-bodied persons and stroke survivors," *IEEE Trans. Biomed. Eng.*, vol. 67, no. 5, pp. 1272–1281, May 2020.
[38] M. A. Oskoei and H. Hu, "Myoelectric control systems—A survey," *Biomed. Signal Process. Control*, vol. 2, no. 4, pp. 275–294, Oct. 2007.
[39] B. Hudgins, P. Parker, and R. N. Scott, "A new strategy for multifunction myoelectric control," *IEEE Trans. Biomed. Eng.*, vol. 40, no. 1, pp. 82–94, Jan. 1993.
[40] M. Hakonen, H. Piitulainen, and A. Visala, "Current state of digital signal processing in myoelectric interfaces and related applications," *Biomed. Signal Process. Control*, vol. 18, pp. 334–359, Apr. 2015.
[41] K. Englehart and B. Hudgins, "A robust, real-time control scheme for multifunction myoelectric control," *IEEE Trans. Biomed. Eng.*, vol. 50, no. 7, pp. 848–854, Jul. 2003.
[42] A. Waris, I. K. Niazi, M. Jamil, O. Gilani, K. Englehart, W. Jensen, M. Shafique, and E. N. Kamavuako, "The effect of time on EMG classification of hand motions in able-bodied and transradial amputees," *J. Electromyogr. Kinesiol.*, vol. 40, pp. 72–80, Jun. 2018.
[43] J. Shen, Y. Qu, W. Zhang, and Y. Yu, "Wasserstein distance guided representation learning for domain adaptation," in *Proc. AAAI Conf. Artif. Intell.*, New Orleans, LA, USA, Feb. 2018, vol. 32, no. 1, pp. 4058–4065.
[44] K. Simonyan and A. Zisserman, "Very deep convolutional networks for large-scale image recognition," in *Proc. ICLR*, San Diego, CA, USA, May 2015, pp. 1–14.
[45] M. Arjovsky, S. Chintala, and L. Bottou, "Wasserstein generative adversarial networks," in *Proc. ICML*, Sydney, NSW, Australia, Aug. 2017, pp. 214–223.
[46] C. Villani, *Optimal Transport: Old and New*. Berlin, Germany: Springer, 2009.
[47] I. Gulrajani, F. Ahmed, M. Arjovsky, V. Dumoulin, and A. C. Courville, "Improved training of Wasserstein GANs," in *Proc. Adv. Neural. Inf. Process. Syst.*, vol. 30, Long Beach, CA, USA, Dec. 2017, pp. 1–11.
[48] J. Cao, K. Zhang, M. Luo, C. Yin, and X. Lai, "Extreme learning machine and adaptive sparse representation for image classification," *Neural Netw.*, vol. 81, pp. 91–102, Sep. 2016.
[49] H. A. Varol, F. Sup, and M. Goldfarb, "Multiclass real-time intent recognition of a powered lower limb prosthesis," *IEEE Trans. Biomed. Eng.*, vol. 57, no. 3, pp. 542–551, Mar. 2010.
[50] K. H. Ha, H. A. Varol, and M. Goldfarb, "Volitional control of a prosthetic knee using surface electromyography," *IEEE Trans. Biomed. Eng.*, vol. 58, no. 1, pp. 144–151, Jan. 2011.
[51] F. Duan, X. Ren, and Y. Yang, "A gesture recognition system based on time domain features and linear discriminant analysis," *IEEE Trans. Cogn. Develop. Syst.*, vol. 13, no. 1, pp. 200–208, Mar. 2021.
[52] E. Bergil, C. Oral, and E. U. Ergul, "Efficient hand movement detection using k-means clustering and k-nearest neighbor algorithms," *J. Med. Biol. Eng.*, vol. 41, no. 1, pp. 11–24, Feb. 2021.
[53] A. C. Turlapaty and B. Gokaraju, "Feature analysis for classification of physical actions using surface EMG data," *IEEE Sensors J.*, vol. 19, no. 24, pp. 12196–12204, Dec. 2019.
[54] M.-F. Lucas, A. Gaufriau, S. Pascual, C. Doncarli, and D. Farina, "Multi-channel surface EMG classification using support vector machines and signal-based wavelet optimization," *Biomed. Signal Process. Control*, vol. 3, no. 2, pp. 169–174, Apr. 2008.
[55] M. Tavakoli, C. Benussi, P. A. Lopes, L. B. Osorio, and A. T. de Almeida, "Robust hand gesture recognition with a double channel surface EMG wearable armband and SVM classifier," *Biomed. Signal Process. Control*, vol. 46, pp. 121–130, Sep. 2018.
[56] F. Amirabdollahian and M. L. Walters, "Application of support vector machines in detecting hand grasp gestures using a commercially off the shelf wireless myoelectric armband," in *Proc. Int. Conf. Rehabil. Robot. (ICORR)*, London, U.K., Jul. 2017, pp. 111–115.
[57] X. Zhai, B. Jelfs, R. H. M. Chan, and C. Tin, "Self-recalibrating surface EMG pattern recognition for neuroprosthesis control based on convolutional neural network," *Frontiers Neurosci.*, vol. 11, pp. 1–11, Jul. 2017.
[58] A. R. Asif, A. Waris, S. O. Gilani, M. Jamil, H. Ashraf, M. Shafique, and I. K. Niazi, "Performance evaluation of convolutional neural network for hand gesture recognition using EMG," *Sensors*, vol. 20, no. 6, p. 1642, Mar. 2020.
[59] K.-T. Kim, C. Guan, and S.-W. Lee, "A subject-transfer framework based on single-trial EMG analysis using convolutional neural networks," *IEEE Trans. Neural Syst. Rehabil. Eng.*, vol. 28, no. 1, pp. 94–103, Jan. 2020.
[60] U. Côté-Allard, G. Gagnon-Turcotte, A. Phinyomark, K. Glette, E. J. Scheme, F. Laviolette, and B. Gosselin, "Unsupervised domain adversarial self-calibration for electromyography-based gesture recognition," *IEEE Access*, vol. 8, pp. 177941–177955, 2020.
[61] U. Côté-Allard, G. Gagnon-Turcotte, A. Phinyomark, K. Glette, E. Scheme, F. Laviolette, and B. Gosselin, "A transferable adaptive domain adversarial neural network for virtual reality augmented EMG-based gesture recognition," *IEEE Trans. Neural Syst. Rehabil. Eng.*, vol. 29, pp. 546–555, 2021.
[62] R. W. Soukoreff and I. S. MacKenzie, "Towards a standard for pointing device evaluation, perspectives on 27 years of Fitts' law research in HCI," *Int. J. Hum.-Comput. Stud.*, vol. 61, no. 6, pp. 751–789, Dec. 2004.
[63] L. H. Smith, T. A. Kuiken, and L. J. Hargrove, "Evaluation of linear regression simultaneous myoelectric control using intramuscular EMG," *IEEE Trans. Biomed. Eng.*, vol. 63, no. 4, pp. 737–746, Apr. 2016.
[64] T. R. Farrell and R. F. Weir, "The optimal controller delay for myoelectric prostheses," *IEEE Trans. Neural Syst. Rehabil. Eng.*, vol. 15, no. 1, pp. 111–118, Mar. 2007.
[65] T. J. Butler, S. L. Kilbreath, R. B. Gorman, and S. C. Gandevia, "Selective recruitment of single motor units in human flexor digitorum superficialis muscle during flexion of individual fingers," *J. Physiol.*, vol. 567, no. 1, pp. 301–309, Aug. 2005.
[66] J. N. A. L. Leijnse, N. H. Campbell-Kyureghyan, D. Spektors, and P. M. Quesada, "Assessment of individual finger muscle activity in the extensor digitorum communis by surface EMG," *J. Neurophysiol.*, vol. 100, no. 6, pp. 3225–3235, Dec. 2008.

**SEJIN KIM** received the B.S. degree in mechanical engineering from Pohang University of Science and Technology (POSTECH), Pohang, South Korea, in 2017, where he is currently pursuing the Ph.D. degree with the Robotics Laboratory. His research interests include biosignal processing and AI-based biorobotics.

**WAN KYUN CHUNG** (Fellow, IEEE) received the B.S. degree in mechanical design from Seoul National University, Seoul, South Korea, in 1981, and the M.S. degree in mechanical engineering and the Ph.D. degree in production engineering from Korea Advanced Institute of Science and Technology, Daejeon, South Korea, in 1983 and 1987, respectively.

In 1987, he joined the School of Mechanical Engineering, Pohang University of Science and Technology, Pohang, South Korea, where he is currently a Professor. In 1988, he was a Visiting Professor with the Robotics Institute, Carnegie Mellon University, Pittsburgh, PA, USA. In 1995, he was a Visiting Scholar with the University of California at Berkeley, Berkeley, CA, USA. His research interests include biomedical robotics, AI-based biorobotics, and the development of robust controllers for precision motion control.

Dr. Chung was the Editor-in-Chief of *Intelligent Service Robotics*.